



# 1 **SILLi 1.0: A 1D Numerical Tool Quantifying the Thermal Effects of Sill** 2 **Intrusions**

3 \*Karthik Iyer<sup>1,2</sup>, Henrik Svensen<sup>3</sup> and Daniel W. Schmid<sup>1,4</sup>

4 \*karthik.iyer@geomodsol.com

5 <sup>1</sup> GeoModelling Solutions GmbH, Zurich, Switzerland

6 <sup>2</sup> GEOMAR, Helmholtz Centre for Ocean Research, Kiel, Germany

7 <sup>3</sup> Centre for Earth Evolution and Dynamics, University of Oslo, Norway

8 <sup>4</sup> Physics of Geological Processes, University of Oslo, Norway

9

## 10 **Abstract**

11 Igneous intrusions in sedimentary basins may have a profound effect on the thermal structure and physical  
12 properties of the hosting sedimentary rocks. These include mechanical effects such as deformation and uplift of  
13 sedimentary layers, generation of overpressure, mineral reactions and porosity evolution, and fracturing and  
14 vent formation following devolatilization reactions and the generation of CO<sub>2</sub> and CH<sub>4</sub>. The gas generation and  
15 subsequent migration and venting may have contributed to several of the past climatic changes such as the  
16 end-Permian event and the Paleocene-Eocene Thermal Maximum. Additionally, the generation and expulsion of  
17 hydrocarbons and cracking of pre-existing oil reservoirs around a hot magmatic intrusion is of significant  
18 interest to the energy industry. In this paper, we present a user-friendly 1D FEM based tool, SILLi, which  
19 calculates the thermal effects of sill intrusions on the enclosing sedimentary stratigraphy. The model is  
20 accompanied by three case studies of sills emplaced in two different sedimentary basins, the Karoo Basin in  
21 South Africa and the Vøring Basin offshore Norway. Input data for the model is the present-day well log or  
22 sedimentary column with an Excel input file and includes rock parameters such as thermal conductivity, total  
23 organic carbon (TOC) content, porosity, and latent heats. The model accounts for sedimentation and burial  
24 based on a rate calculated by the sedimentary layer thickness and age. Erosion of the sedimentary column is



25 also included to account for realistic basin evolution. Multiple sills can be emplaced within the system with  
26 varying ages. The emplacement of a sill occurs instantaneously. The model can be applied to volcanic  
27 sedimentary basins occurring globally. The model output includes the thermal evolution of the sedimentary  
28 column through time, and the changes that take place following sill emplacement such as TOC changes, thermal  
29 maturity, and the amount of organic and carbonate-derived CO<sub>2</sub>. The TOC and vitrinite results can be readily  
30 benchmarked within the tool to present-day values measured within the sedimentary column. This allows the  
31 user to determine the conditions required to obtain results that match observables and leads to a better  
32 understanding of metamorphic processes in sedimentary basins.

33

## 34 **1 Introduction**

35 Volcanic processes can strongly influence the development of sedimentary basins associated with continental  
36 margins. Magmatic bodies such as dikes and sills have a major impact on the thermal evolution of these  
37 sedimentary basins. The short-term effects of igneous intrusions include deformation and uplift of the intruded  
38 sediments, heating of the host rock, mineral reactions, generation of petroleum, boiling of pore fluids and  
39 possible hydrothermal venting (Jamtveit et al., 2004; Malthe-Sorensen et al., 2004; Svensen et al., 2004; Wang  
40 et al., 2012b). Long-term effects include focused fluid flow, migration of hydrothermal and petroleum products,  
41 formation of mechanically strong dolerite and hornfels in the contact aureole and differential compaction (Iyer  
42 et al., 2013; Iyer et al., 2017; Kjoberg et al., 2017; Planke et al., 2005). This is of particular importance to  
43 understanding the carbon cycle, as thermal stresses, besides those associated with burial, encountered by  
44 organic matter in immature source rocks will determine the ultimate production and fate of the CO<sub>2</sub> and CH<sub>4</sub>  
45 generated. Vent structures are intimately associated with sill intrusions in sedimentary basins globally and are  
46 thought to have been formed contemporaneously due to overpressure generated by pore-fluid boiling gas  
47 generation during thermogenic breakdown of kerogen (Aarnes et al., 2015; Iyer et al., 2017; Jamtveit et al.,  
48 2004). Methane and other gases generated during this process may have driven catastrophic climate change in  
49 the geological past (Svensen and Jamtveit, 2010; Svensen et al., 2009). In order to understand these problems,  
50 numerical models are widely used to reconstruct the thermal history of a basin where only a few of these  
51 parameters are known.



52 A number of analytical and numerical models have been developed that study the thermal effects of igneous  
53 intrusions dating back to the early- and mid-1900's (Jaeger, 1964; Jaeger, 1957, 1959; Lovering, 1935).  
54 Subsequent 1D and 2D models added additional complexity to the models by the addition of emplacement  
55 mechanisms and timing, source rock maturation, hydrocarbon generation, latent heats of devolatilization and  
56 maturation, fluid processes and overpressure generation (Aarnes et al., 2011a; Fjeldskaar et al., 2008;  
57 Galushkin, 1997; Iyer et al., 2017; Monreal et al., 2009; Wang, 2012; Wang et al., 2010; Wang and Song, 2012;  
58 Wang et al., 2012a). Contact metamorphic processes are well understood (e.g. (Aarnes et al., 2010; Jamtveit et  
59 al., 1992; Tracy and Frost, 1991)), but many published papers do not take into account the basin history or the  
60 variations in contact aureole thickness that arise from the type of measuring method that has been used. In  
61 general, the contact metamorphic effects depend on 1) sill thickness (note that dikes cannot be directly  
62 compared with sills), 2) sill emplacement temperature, 3) thermal gradient and emplacement depth (i.e.  
63 temperature and background maturation), 4) emplacement history (instantaneous versus prolonged magma  
64 flow), 5) host rock composition and characteristics (such as thermal conductivity, organic carbon content,  
65 porosity, permeability) and 6) conductive versus advective cooling (e.g. (Aarnes et al., 2010; Galushkin, 1997;  
66 Iyer et al., 2013; Iyer et al., 2017; Jaeger, 1964; Lovering, 1935; Wang, 2012)). In addition, the contact aureole  
67 width depends on how aureoles are studied and measured. The aureole thickness depends on the proxy used,  
68 including sonic velocity, density, mineralogy and mineral properties, magnetic susceptibility, total organic  
69 carbon content, vitrinite reflectivity, color, porosity, or organic geochemistry. Note that these aureole thickness  
70 proxies will not necessarily give the same result. Finally, the aureole thickness also depends on the proximity to  
71 other sills emplaced at the same time (see Aarnes et al. (2011b) for a quantification).

72 In this paper we present a generic 1D thermal model, SILLi, which can be applied to studying the thermal effects  
73 of sill intrusions in sedimentary basins globally. Besides heat transfer, the model also accounts for the  
74 sequential deposition of sedimentary layers through time, erosion, latent heat effects and gas generation by  
75 decarbonation reactions and organic matter maturation. The model results can be then easily compared to the  
76 two most widely used aureole proxies in sedimentary rocks, vitrinite reflectance (VR) and total organic carbon  
77 (TOC) data.

78



## 79 **2 Model Input**

80 The one dimensional, Finite Element Method (FEM) model numerically recreates the thermal effects of sill  
81 emplacement in a sedimentary column. The model is written using MATLAB and requires version 2014b or  
82 higher to run. The model input is specified in an Excel (\*.xls) file and is read by the Matlab file, SILLi.m. The user  
83 also specifies the model resolution with the igneous intrusions and sedimentary layers by giving the minimum  
84 spacing (m) or the minimum number of points in the Matlab file. The measure that produces the highest  
85 resolution is used. The Excel file is composed of seven tabs outlined below. If a previously calculated output file  
86 is available for the input file, the program prompts the user to choose between loading the output file for  
87 further analysis and performing a new calculation which overwrites the existing file.

88 For correct model use, the geological input needs to be based on either a borehole (with horizontal  
89 stratigraphy) or an outcrop that is converted into a pseudo-borehole. If the case study is outcrop-based, a  
90 pseudo-borehole stratigraphy should be constructed including the regional basin stratigraphy. Note that  
91 sedimentary rocks present at higher stratigraphic levels elsewhere in the basin should be added to the erosion  
92 history of the basin. Moreover, the sills (and samples) should be rotated back to horizontal if the stratigraphy  
93 was tilted post sill emplacement. Using TOC and VR data from sedimentary rocks outside the immediate contact  
94 aureoles will improve the model calibration.

95

### 96 **2.1 Fluid**

97 This tab contains three columns describing the fluid name, its density ( $\text{kg/m}^3$ ) and its heat capacity ( $\text{J/kg/K}$ ).

98

### 99 **2.2 Lithology**

100 This tab contains the data required for the model to build the present-day sedimentary column. The various  
101 columns detail the name of the sedimentary layer (character only) and various material properties such as  
102 density ( $\text{kg/m}^3$ ), heat capacity ( $\text{J/kg/K}$ ), porosity (fraction), thermal conductivity ( $\text{W/m/K}$ ), initial TOC content  
103 (wt%) and latent heats of organic maturation and dehydration ( $\text{kJ/kg}$ ). Information regarding the kind of  
104 carbonate contained in the sedimentary layer can be given in the last column if decarbonation reactions are



105 considered. The mineral constitution of the carbonate can be chosen as marl (1), dolomite (2) or  
106 dolomite/evaporite mix (3). A zero (0) is entered in this column if decarbonation reactions are not required. The  
107 lithology tab also contains columns where the present-day top depth (m) and age (Ma) of each layer can be  
108 given which determine the depositional sequence and sedimentation rate for the layer (see Section 3.1). Note  
109 that the ages of the sedimentary must be unique. A hypothetical basement is added 10 m below the deepest  
110 sedimentary layer top depth or 300 m below the bottom of the deepest sill intrusion, whichever is deeper.

111

## 112 **2.3 Erosion**

113 This tab is similar to the lithology tab and contains information on eroded layers. Additional columns in this tab  
114 contain information regarding the erosion timing (Ma) and the thickness of the eroded layer (m). Note that the  
115 top depth of the eroded layer must coincide with the top of a sedimentary layer in the lithology tab. If part of  
116 sedimentary layer is indeed eroded before deposition continues (i.e. the eroded layer lay inside a deposited  
117 layer), the layer needs to be considered as unique layers separated by the eroded layer. Multiple eroded layers  
118 can have the same top depths provided that older layers with the same top depth are eroded first. Similarly,  
119 eroded layers have to be eroded first prior to deposition of younger layers. The ages of the eroded layers  
120 cannot coincide with other layers.

121

## 122 **2.4 Sills**

123 This tab contains information necessary for the emplacement of sill intrusions. The top depth (m) and thickness  
124 (m) of the sill constrain the geometry of the intrusion. Additional information includes the time of emplacement  
125 (Ma), emplacement temperature (°C), melt and solid densities ( $\text{kg/m}^3$ ), melt and solid heat capacities ( $\text{J/kg/K}$ ),  
126 thermal conductivity ( $\text{W/m/K}$ ), solidus and liquidus temperatures of the magma (°C) and the latent heat of  
127 crystallization ( $\text{kJ/kg}$ ). The emplacement of the intrusion is assumed to be instantaneous. Note that the top  
128 depth of the sill cannot be the same as the top depth of a sedimentary layer. On the same note, the top depth  
129 of a sedimentary layer cannot be inside a sill intrusion. Emplacement ages cannot exactly coincide with layer  
130 ages.



131

## 132 **2.5 Temperature Data**

133 This tab contains temperature data (°C) vs. depth (m) for the sedimentary column. The data in this tab is used to  
134 construct a geothermal gradient by using the best linear fit and therefore needs to contain at least two data  
135 points. Additionally, the first data point must coincide with the column top describing the surface temperature.

136

## 137 **2.6 Vitrinite Data (Optional)**

138 This tab contains present day vitrinite reflectance data presented in depth (m) and VR values (%Ro). Standard  
139 deviation of the values when available can be included. This data is used for comparison of the modelled VR  
140 values to observations. This tab can be left blank if no information is available.

141

## 142 **2.7 TOC Data (Optional)**

143 This tab contains present day TOC content data (wt%) vs. depth (m) measured in the sedimentary column which  
144 is used to compare to the model results. This tab can be left blank if no information is available.

145

# 146 **3 Method**

## 147 **3.1 Sediment Deposition and Erosion**

148 Each sedimentary layer, including the eroded layers, is deposited sequentially in time based on the depositional  
149 age. The rate of sedimentation for each layer is determined by the thickness of the layer and the difference in  
150 time between its top age and that of the layer deposited before it. Erosional layers in the sedimentary column  
151 are deposited in the same way as other layers. Erosion of the entire layer occurs within a single step at the  
152 specified erosion age. The temperature boundary conditions are accordingly adjusted for the height of the new  
153 sedimentary column. Note that the bottom boundary is extended to 5 times the thickness of the bottommost  
154 sill if that sill is close to or at the bottom boundary in order to remove boundary effects.



155

## 156 3.2 Thermal Diffusion

157 The thermal solver computes the temperature within the deposited sedimentary column by applying fixed  
158 temperatures at the top and bottom at every step which are calculated from the prescribed geotherm (see  
159 Section 2.5) and the energy diffusion equation,

$$160 \quad \left[ \phi \rho_f c_{pf} + (1 - \phi) \rho_r c_{peff} \right] \frac{\partial T}{\partial t} = \nabla \cdot (\kappa \nabla T) \quad (1)$$

161 Table 1 contains the definitions of all the notations used in the manuscript. The effective rock heat capacity  
162 accounts for the latent heat of fusion in the crystallizing parts of the sill between the solidus ( $T_s$ ) and liquidus  
163 ( $T_L$ ) temperature of the magma (e.g. (Galushkin, 1997))

$$164 \quad c_{peff} = c_{pm} \left[ 1 + \frac{L_c}{(T_L - T_s) c_{pm}} \right] \text{ if } [T_s < T < T_L] \quad (2)$$
$$c_{peff} = c_{pr} \quad \text{ if } [T_s > T]$$

165 Sills are emplaced instantaneously at the specified time and temperature within the sedimentary column. The  
166 emplacement of multiple sills in the same step is possible. The time-steps used for thermal diffusion after sill  
167 emplacement are automatically calculated based on the sill thickness and the characteristic time required for  
168 thermal diffusion. The time step is initially small in order to accurately resolve the thermal evolution of the  
169 contact aureole around the sill and is gradually increased once the energy released by the cooling sill is  
170 dissipated.

171 Dehydration reactions in the host rock are implemented by modifying the thermal diffusion equation when  
172 temperatures of the sediments increase within a certain range (Galushkin, 1997; Wang, 2012)

$$173 \quad \left[ \phi \rho_f c_{pf} + (1 - \phi) \rho_r c_{peff} \right] \frac{\partial T}{\partial t} = \nabla \cdot (\kappa \nabla T) - H \quad (3)$$



174

$$H = \frac{(1-\phi)\rho_r L_d}{T_{d1} - T_{d2}} \frac{\partial T}{\partial t} \quad (4)$$

<b>Symbol</b>	<b>Description</b>	<b>Units</b>
$A$	Frequency factor	$s^{-1}$
$c_{peff}$	Effective rock heat capacity	$J\ kg^{-1}\ K^{-1}$
$c_{pf}$	Fluid heat capacity	$J\ kg^{-1}\ K^{-1}$
$c_{pr}$	Rock heat capacity	$J\ kg^{-1}\ K^{-1}$
$E$	Activation energy	$KJ\ mol^{-1}$
$f$	Stoichiometric factor	
$F$	Reaction extent	
$g$	Gravitational acceleration	$m\ s^{-2}$
$i$	Reactive component	
$L_c$	Latent heat of crystallization	$KJ\ kg^{-1}$
$m_{CO_2}$	Carbon to CO <sub>2</sub> conversion factor	3.66
$P_{atm}$	Atmospheric pressure	$10^5\ Pa$
$P_{H_2O}$	Hydrostatic pressure	Pa
$R_{CO_2}$	Rate of CO <sub>2</sub> generation	$kg\ m^{-3}\ s^{-1}$
$R_{om}$	Rate of organic matter degradation	$kg\ m^{-3}\ s^{-1}$
$t$	Time	s
$T_L$	Liquidus temperature	°C
$T_S$	Solidus temperature	°C
$T$	Temperature	°C
$T_{d2} - T_{d1}$	Temperature range for dehydration reactions (Galushkin, 1997)	350-650 °C
$w$	Amount of reactive component	Fraction
$Z$	Depth	km
$\phi$	Rock porosity	Fraction





$\kappa$	Conductivity	$\text{W m}^{-1} \text{K}^{-1}$
$\rho_f$	Fluid density	$\text{kg m}^{-3}$
$\rho_r$	Rock density	$\text{kg m}^{-3}$

175 *Table 1. Definition of symbols used in the model.*

176

### 177 3.3 Thermal Maturation of Organic Matter

178 Vitrinite reflectance is a widely used indicator of thermal maturity and can be readily measured in the field. One  
 179 of the most common methods used to calculate the thermal maturity of the source rock is the EASY%Ro  
 180 method put forward by Sweeney and Burnham (1990). This model uses 20 parallel Arrhenius-type of first order  
 181 reactions to describe the complex process of kerogen breakdown due to temperature increase. The reaction for  
 182 the  $i^{\text{th}}$  component is given by

$$183 \quad \frac{dw_i}{dt} = -w_i A \exp\left[-\frac{E_i}{RT^t}\right] \quad (5)$$

184 where  $w_i$  is the amount of material for component  $i$ ,  $E_i$  is the activation energy for the given reaction and  $T^t$  is  
 185 time-dependent temperature.

186 The total amount of material reacted is obtained by summing up the individual reactions

$$187 \quad \frac{dw}{dt} = \sum_i \frac{dw_i}{dt} \quad (6)$$

188 The fraction of reactant converted is

$$189 \quad F = 1 - \frac{w}{w_0} = 1 - \sum_i f_i \left( \frac{w_i}{w_{0i}} \right) \quad (7)$$

190 from which the vitrinite reflectance can be readily calculated by



191 
$$\%Ro = \exp(-1.6 + 3.7F) \quad (8)$$

192 The amount of TOC that has reacted for any given time can be calculated by

193 
$$TOC(t) = TOC_o F(t) \quad (9)$$

194 and the rate of organic matter degradation by

195 
$$R_{om} = (1 - \phi) \rho_r \frac{\partial TOC}{\partial t} \quad (10)$$

196 The maximum amount of TOC that can be reacted by this method is 85% of the initial total. Note that in the  
197 inner part of the contact aureole close the sill, data shows that all of the organic matter has been reacted or  
198 removed (eg. LA1/68 in section 5.2.2). We assume that all of the hydrocarbons released during thermal  
199 degradation are converted into carbon dioxide. The amount of organic carbon dioxide generated ( $R_{CO_2}$ ) for a  
200 time step is given by

201 
$$R_{CO_2} = R_{om} m_{CO_2} \quad (11)$$

202 where  $m_{CO_2}$  is a stoichiometric conversion factor (3.67) to transform carbon into carbon dioxide. Note that  
203 metamorphism of sedimentary rocks will generate  $CH_4$  (e.g., (Aarnes et al., 2010; Iyer et al., 2017)), but in our  
204 model the reacted carbon is recalculated to  $CO_2$ . If needed, the  $CO_2$  model output can be easily converted to  
205 either C or  $CH_4$ .

206 The latent heat of organic maturation is accounted for in the energy equation

207 
$$\left[ \phi \rho_f c_{pf} + (1 - \phi) \rho_r c_{peff} \right] \frac{\partial T}{\partial t} = \nabla \cdot (\kappa \nabla T) - H - L_{om} R_{om} \quad (12)$$

208

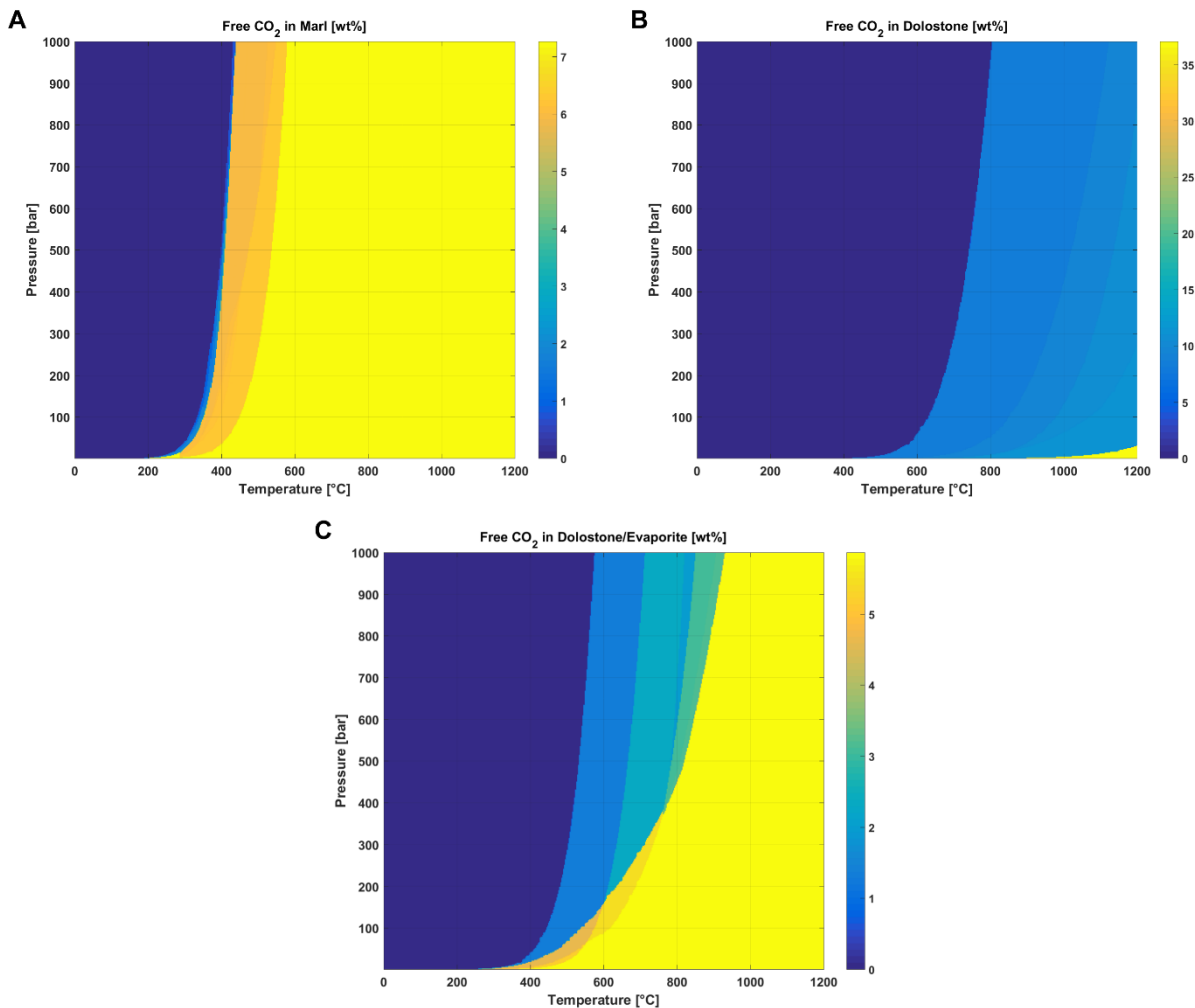
### 209 3.4 Mineral Decarbonation

210 Carbonate minerals undergo decarbonation reactions as they are heated to high temperatures. This results in  
211 mineral transformations and the release of inorganic carbon dioxide which may significantly add to the  $CO_2$



212 budget associated with igneous intrusions. The amount of inorganic CO<sub>2</sub> liberated during metamorphic  
 213 transformation over a range of temperature and fluid pressure for marl, dolomite and dolomite/evaporite  
 214 mixture is pre-computed as a phase diagram using Perple\_X (Connolly and Petrini, 2002) (Figure 1). The model  
 215 evaluates the total amount of inorganic CO<sub>2</sub> liberated by carbonate layers based on the temperature and  
 216 pressure evolution of the layer through time within the phase diagrams. Fluid pressure within the sedimentary  
 217 column is calculated by integrating the rock density over depth in addition to atmospheric pressure:

$$218 \quad P_{H_2O} = P_{atm} + \int_{Z_{min}}^{Z_{max}} \rho_f \bar{g} \quad (13)$$



219



220 *Figure 1. Phase diagrams generated by Perple\_X showing the amounts of inorganic CO<sub>2</sub> liberated with respect to*  
221 *temperature and pressure for marl (A), dolostone (B) and dolostone/evaporite (C).*

222

### 223 **3.5 Model Mesh and Time-Stepping**

224 The entire sedimentary column including the eroded layers and igneous intrusions is reconstructed and the  
225 column nodes and elements for the FEM model are generated using the user-specified resolution. The nodes  
226 are initially collapsed onto each other in depth. Each sedimentary node is assigned a time during which it is  
227 expanded (or deposited) within the sedimentary column based on the layer age and its thickness. All of the  
228 elements and nodes associated with each igneous intrusion are expanded simultaneously during the  
229 corresponding emplacement time. Eroded layers are removed in a single time step specified by the erosion age  
230 and the corresponding nodes are collapsed. In order to correctly capture thermal diffusion across the large  
231 thermal gradient adjacent to a hot intrusion, the time step is initially very small and exponentially increases  
232 during the heating period after sill emplacement and before the next depositional event. The heating period of  
233 the sill, over which the exponential time sub-stepping is used, is analytically determined from the characteristic  
234 diffusion time for the sill thickness (Jaeger, 1959).

### 235 **3.6 Model Limitations**

- 236 • The model is one-dimensional and will therefore not resolve thermal effects that would require a full 3D  
237 model.
- 238 • The model does not account for advective transport of heat through the system by fluids. However,  
239 previous models have shown that this process would be dominant only in high permeability systems or  
240 at the sill edges/tips in low permeability systems (Iyer et al., 2013; Iyer et al., 2017). Therefore, the  
241 model presented in this manuscript works well for relatively low permeability systems with shales,  
242 mudstone etc. and when the sedimentary column passes through the sill interior away from the edges.
- 243 • The model does not account for other mineral reactions in the contact aureole besides decarbonation  
244 of carbonates. The various mineral reactions possible in the contact aureole can be implemented as an  
245 add-on module to the model if needed.
- 246 • The model assumes that TOC conversion in all types of sedimentary rocks can be estimated by using the  
247 EASY%Ro method with a maximum conversion value of 85%. Although, this is a good first  
248 approximation, it cannot account for the complete loss of carbon in zones very close to the sill-host rock  
249 interface which would result in an underestimation of the released gases (Svensen et al., 2015). On the



250 other hand, the provenance of the sedimentary rock can also significantly affect how kerogen present in  
 251 organic matter reacts to form hydrocarbons which may result in a reduction in the amount of  
 252 convertible organic matter due to the presence of inert kerogen (Iyer et al., 2017; Pepper and Corvi,  
 253 1995).

## 255 4 Model Output

256 The model input and results are presented with the help of a GUI (Section 4.6). Model data are written out as a  
 257 single .mat (Matlab data) file in the same directory as the user-defined path for the input Excel file and with the  
 258 same filename. The file contains five 'struct' variables of which three contain input information (rock, sill and  
 259 welldata) and the other two contain model results (result and release). The structure of the variables are  
 260 described below.

### 262 4.1 Struct Variable: rock

263 This variable contains input information on the sedimentary layers in the column including the eroded layers.  
 264 The information is saved as variables given in Table 2 and is sorted according to their top depths. Note that top  
 265 depths are corrected for the eroded layers that are also included.

<b>Variable Name</b>	<b>Description</b>
<b>Name</b>	User-defined names of all the sedimentary layers in the column.
<b>num</b>	Total number of deposited sedimentary layers.
<b>top</b>	Top depth of the shallowest sedimentary layer.
<b>bot</b>	Top depth of the deepest sedimentary layer.
<b>Tops</b>	Top depths of sedimentary layers.
<b>Ages</b>	Ages of sedimentary layers.
<b>Rho</b>	Density of sedimentary layers.
<b>Cp</b>	Heat capacity of sedimentary layers.
<b>Phi</b>	Porosity of sedimentary layers.



<b>K</b>	Thermal conductivity of sedimentary layers.
<b>Toc</b>	TOC content of sedimentary layers.
<b>Lm</b>	Latent heat of maturation of sedimentary layers.
<b>Ld</b>	Latent heat of dehydration of sedimentary layers.
<b>Carb</b>	Carbonate layer identifier (0-3).
<b>Ero_t</b>	Erosion age of sedimentary layers (NaN if layer is not eroded).
<b>Ero_thick</b>	Eroded thickness of sedimentary layers (NaN if layer is not eroded).
<b>Ero_tops</b>	Top depths of the eroded layers only.

266 *Table 2. List of variables in 'rock' struct variable of the output file.*

267

## 268 **4.2 Struct Variable: sill**

269 This variable contains input information on sill intrusions in the column. The information is saved as variables  
270 given in Table 3 and is sorted according to their top depths.

<u>Variable Name</u>	<u>Description</u>
<b>num</b>	Total number of sill intrusions.
<b>Tops</b>	Top depths of sill intrusions.
<b>E_time</b>	Emplacement ages of sill intrusions.
<b>E_temp</b>	Emplacement temperatures of sill intrusions.
<b>Rhom</b>	Melt density of sill intrusions.
<b>Cpm</b>	Melt heat capacity of sill intrusions.
<b>Rhos</b>	Solid density of sill intrusions.
<b>Cps</b>	Solid heat capacity of sill intrusions.
<b>K</b>	Thermal conductivity of sedimentary layers.
<b>Sol</b>	Solidus of melt in sill intrusions.
<b>Liq</b>	Liquidus of melt in sill intrusions.
<b>Ld</b>	Latent heat of crystallization of melt in sill intrusions.



271 *Table 3. List of variables in 'sill' struct variable of the output file.*

272

### 273 **4.3 Struct Variable: welldata**

274 This variable contains input information on measured TOC, VR and temperature data for the sedimentary  
 275 column. The information is saved as variables given in Table 4.

<u>Variable Name</u>	<u>Description</u>
<b>TOC</b>	Measured TOC data vs. depth.
<b>VR</b>	Measured VR data vs. depth.
<b>T</b>	Measured temperature data vs. depth.

276 *Table 4. List of variables in 'welldata' struct variable of the output file.*

277

### 278 **4.4 Struct Variable: result**

279 This variable contains the model results which are saved for every time step when applicable, i.e. variables that  
 280 change over time have rows corresponding to the element or node number (depending on where they are  
 281 defined) and columns corresponding to the time step number. The information is saved as variables given in  
 282 Table 5.

<u>Variable Name</u>	<u>Description (Rows x Columns)</u>
<b>nel</b>	Number of elements in the model (1 x 1)
<b>nnod</b>	Number of nodes in the model (1 x 1)
<b>Gcoord_c</b>	Depth of element centers (1 x no. of elements)
<b>Ind</b>	Internal nodal indexing of sedimentary layers and intrusions (no. of nodes x 1). Intrusions are negatively indexed.
<b>Ind_nel</b>	Internal element indexing of sedimentary layers and intrusions (no. of elements x 1). Intrusions are negatively indexed.
<b>Ind_carb</b>	Nodal indexing of carbonate layers (0-3) (no. of nodes x 1).



<b>Gcoord</b>	Depth of nodes (no. of nodes x no. of time steps).
<b>Temp</b>	Nodal temperature (no. of nodes x no. of time steps).
<b>Pres</b>	Nodal hydrostatic pressure (no. of nodes x no. of time steps).
<b>Toc</b>	Remaining Toc content at nodes (no. of nodes x no. of time steps).
<b>CO2_org</b>	Organic carbon dioxide generated at nodes (no. of nodes x no. of time steps).
<b>Ro</b>	VR at nodes (no. of nodes x no. of time steps).
<b>Tmax</b>	Maximum temperature experienced at nodes (no. of nodes x no. of time steps).
<b>Active</b>	Binary index of 'deposited/expanded' nodes (no. of nodes x no. of time steps).
<b>CO2_release</b>	Inorganic carbon dioxide generated at nodes (no. of nodes x no. of time steps).
<b>Time</b>	Year count for time step (no. of time steps x 1).

283 Table 5. List of variables in 'result' struct variable of the output file.

284

#### 285 4.5 Struct Variable: release

286 This variable contains the amounts of CO<sub>2</sub> released for every time step normalized to rock volume. The  
287 information is saved as variables given in Table 6.

<u>Variable Name</u>	<u>Description (Rows x Columns)</u>
<b>CO2_org</b>	Organic carbon dioxide generated in elements normalized to rock volume (no. of elements x no. of time steps).
<b>CO2_rel</b>	Inorganic carbon dioxide generated in elements normalized to rock volume (no. of elements x no. of time steps).

288 Table 6. List of variables in 'release' struct variable of the output file.

289

#### 290 4.6 Output Graphical User Interface (GUI)

291 The GUI presented during and after the model run contains three tabs containing graphical representations of  
292 the input data, time evolution of model results and CO<sub>2</sub> release through time. An explanation of the tabs is

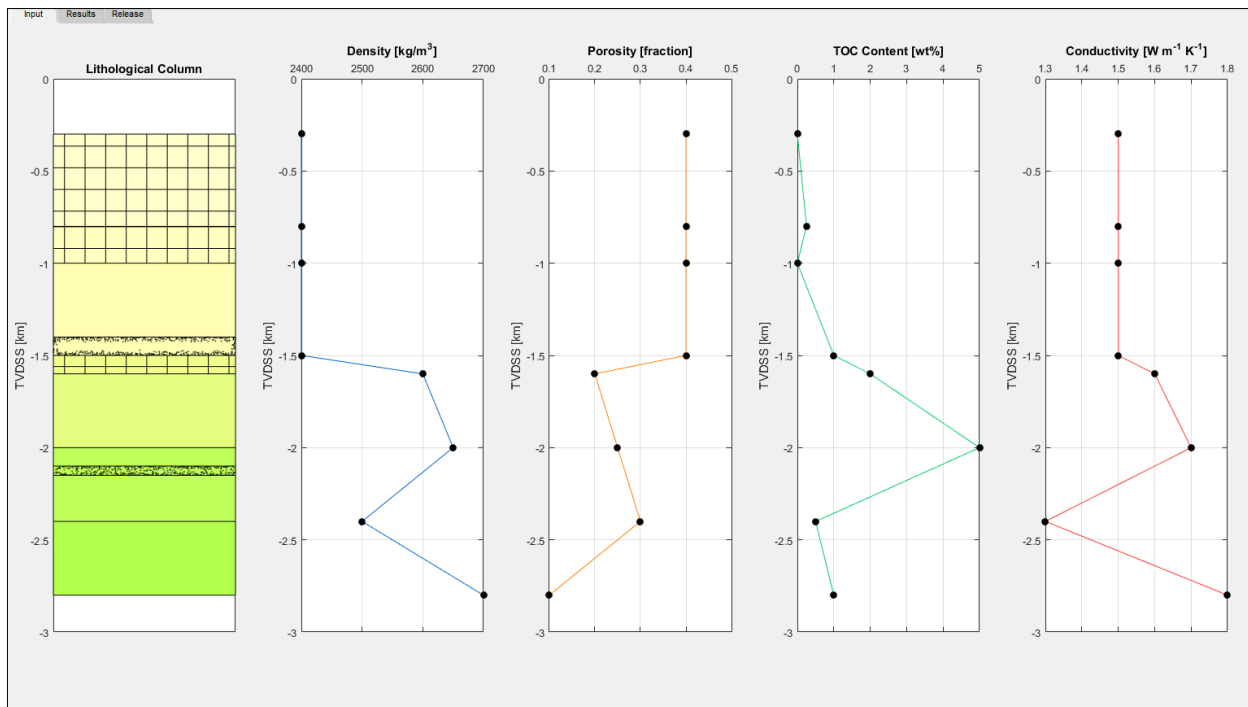




293 given below using a hypothetical test case consisting of a sedimentary column with two sill intrusions and three  
294 eroded layers.

#### 295 4.6.1 Input Tab

296 The left-most subplot of the input tab contains the reconstructed sedimentary column where the layers are  
297 colored according to their depositional age (<http://www.stratigraphy.org/index.php/ics-chart-timescale>) (Figure  
298 2). The sedimentary column also contains eroded layers (hatched) and sill intrusions (speckled). The name and  
299 depositional age of a layer can be found by right-clicking the layer. The other subplots in the input tab contain  
300 information on the density, porosity, initial TOC content and thermal conductivity of the sedimentary layers.  
301 The values of these variables are plotted at the corresponding layer top depth.

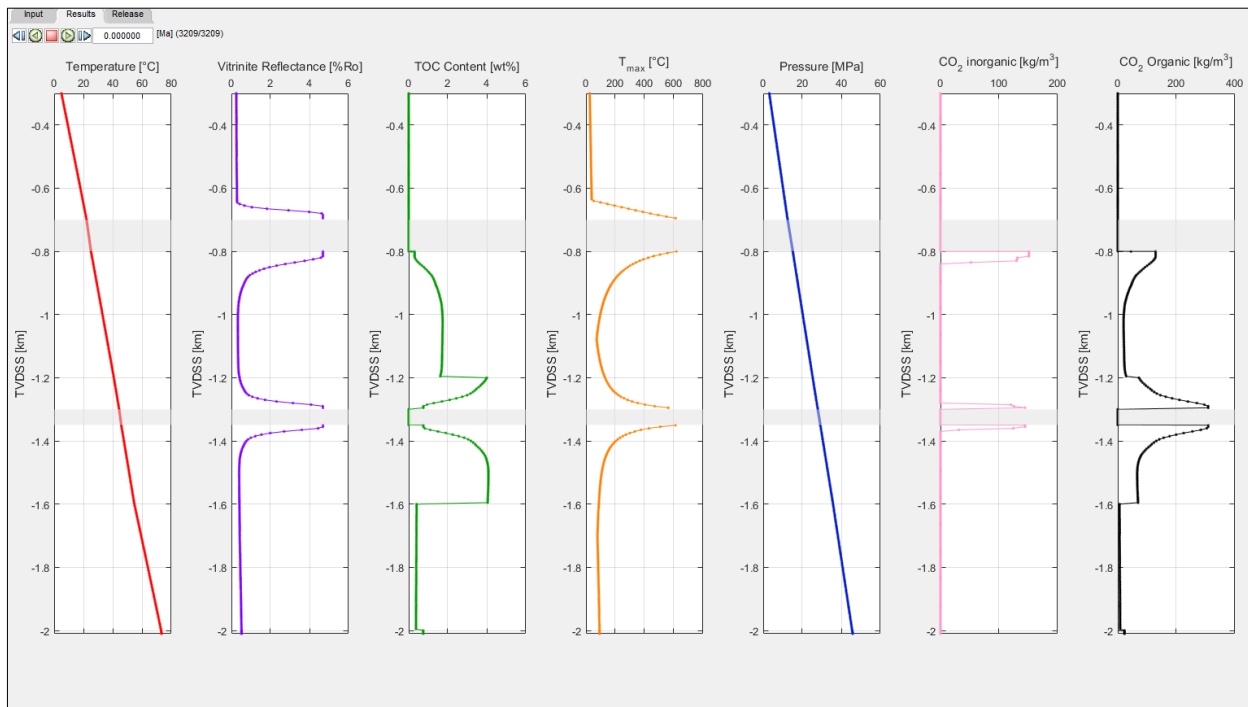


302  
303 *Figure 2. Snapshot of the input tab generated for a hypothetical sedimentary column with two sill intrusions and*  
304 *three eroded layers. Right-clicking a layer in the sedimentary column provides the name and*  
305 *depositional/erosional age of the layer.*



## 306 4.6.2 Results Tab

307 The results tab consists of the evolution of temperature, vitrinite reflectance, TOC content, maximum  
308 temperature, hydrostatic pressure, inorganic and organic CO<sub>2</sub> release within the sedimentary column over  
309 simulated time (Figure 3). The evolution of these variables can be played or stepped through using the player  
310 controls in the top left corner. Alternatively, the user can jump directly to the desired geological time by  
311 inputting it in the player control. Note that this results in the plot jumping to the time-step nearest the desired  
312 time input. Regions containing sill intrusions are highlighted in gray. Users can copy plot data at any time step  
313 by right-clicking the curve.



314

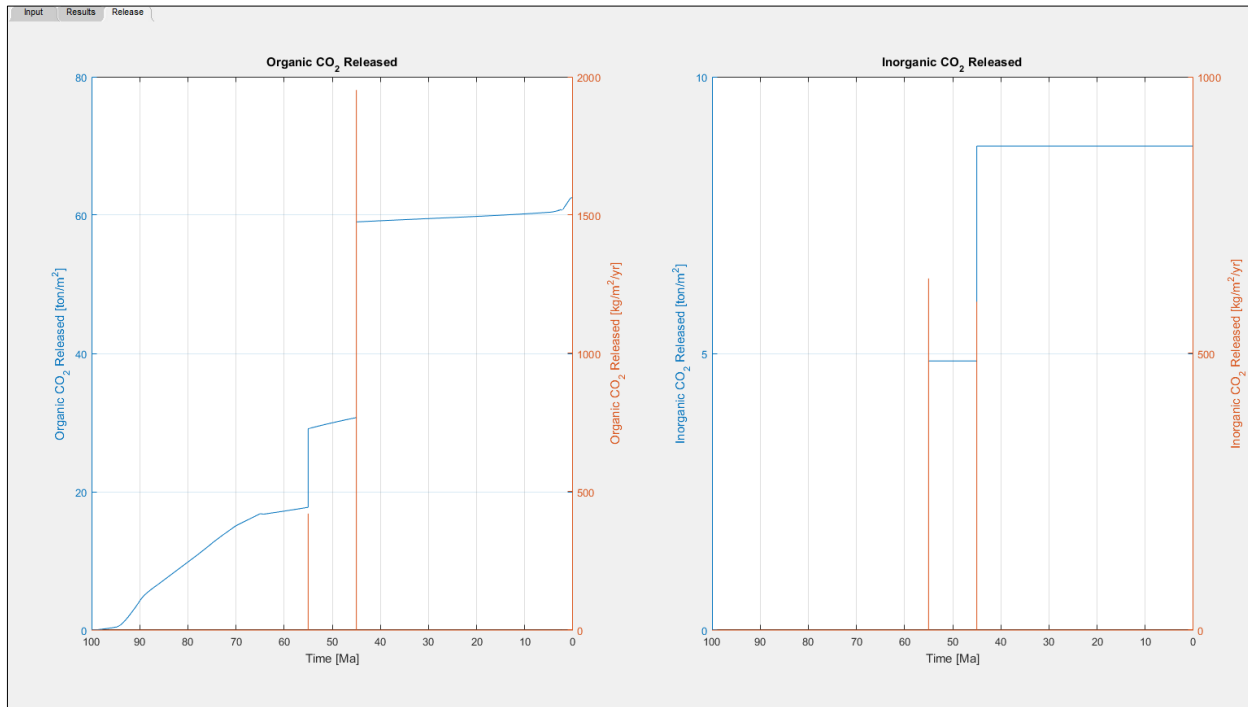
315 *Figure 3. Snapshot of the results tab generated for a hypothetical sedimentary column with two sill intrusions*  
316 *and three eroded layers. Right-clicking any curve allows the user to copy curve data.*

## 317 4.6.3 Release Tab

318 The release tab plots the cumulative and rates of release of organic and inorganic CO<sub>2</sub> due to heating of the  
319 sedimentary layer by sill intrusions (Figure 4). The cumulative and release rates are summed over the entire  
320 sedimentary column. The user can use the cumulative amount of gas released to easily upscale to basin scales



321 by multiplying the value by the area affected by sill intrusions. Users can copy plot data at any time step by  
322 right-clicking the curve.



323  
324 *Figure 4. Snapshot of the release tab generated for a hypothetical sedimentary column with two sill intrusions*  
325 *and three eroded layers. Right-clicking any curve allows the user to copy curve data.*

326

## 327 5 Examples

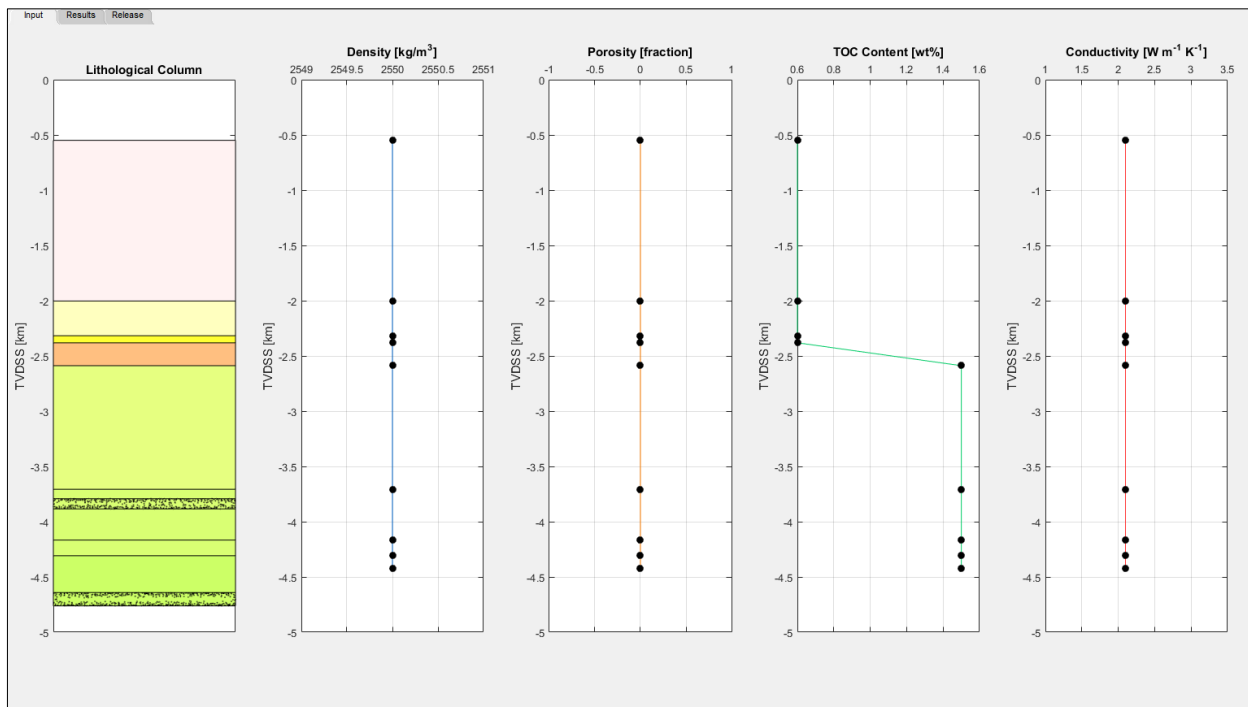
328 The examples below are provided with the code and are used to benchmark observations to model results.

### 329 5.1 Utgard High

330 The Utgard sill complex is part of the North Atlantic Igneous Province (NAIP) in the Vøring and Møre Basins,  
331 offshore Norway. This region underwent massive volcanic activity at the Paleocene-Eocene boundary around  
332 ~55 Ma (Aarnes et al., 2015). The Utgard High borehole 6607/5-2 was drilled through two sills emplaced in the  
333 Upper Cretaceous sedimentary layers. The drilled lithological column consists of nine layers with the oldest

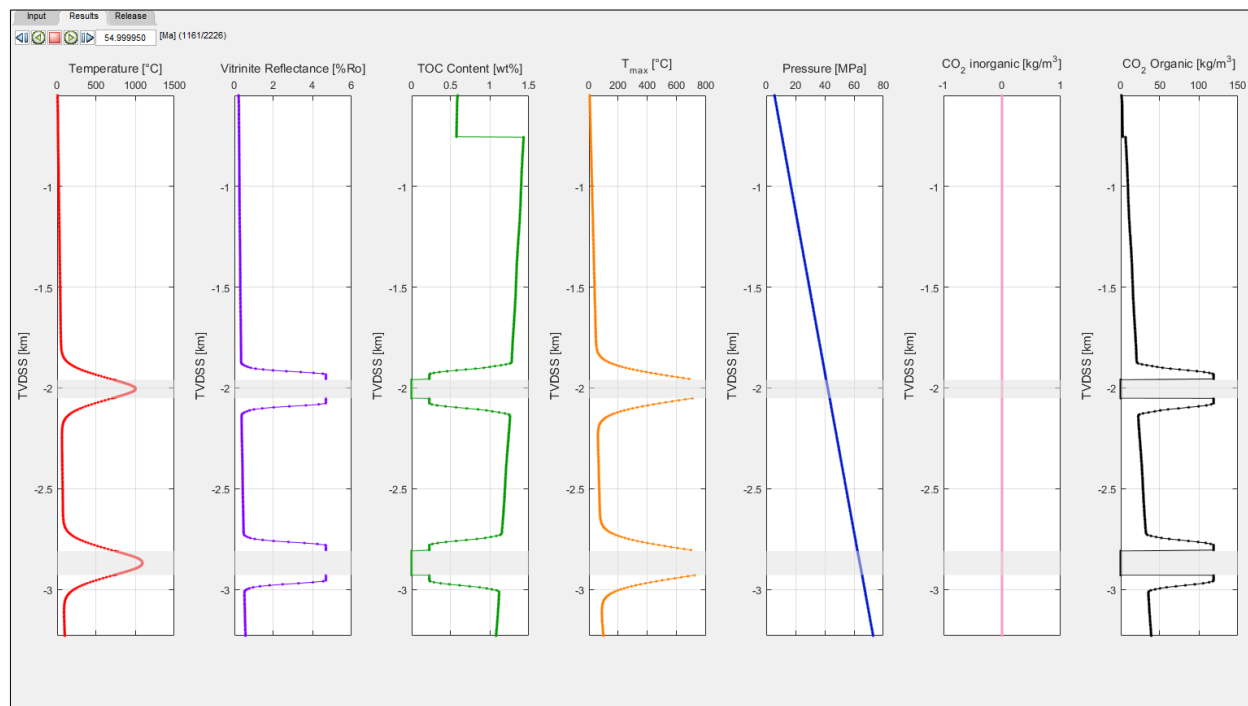


334 being deposited 100 Ma (NPD Factpages, <http://factpages.npd.no/factpages/>) (Figure 5). For simplicity, the  
335 material properties of the entire sedimentary column is set to constant values with the exception of TOC  
336 content. TOC content of the Paleocene and Upper Cretaceous sedimentary layers are set to an initial value of  
337 0.6 and 1.5 wt%, respectively. Carbonate and erosional layers are not considered. The modelled sedimentary  
338 layers are sequentially deposited at the sedimentation rate calculated from the layer top ages. The two sills are  
339 emplaced simultaneously within the Nise and Kvitnos Formations at 55 Ma at a temperature of 1150°C.  
340 Sedimentary rocks around the emplaced sills are progressively heated as the sills cool. The vitrinite reflectance  
341 values increase and the TOC content reduced by thermally degrading organic matter to form CO<sub>2</sub> (Figure 6).  
342 Sedimentation after sill emplacement results in further burial and extension to produce the present-day  
343 sedimentary column. Vitrinite reflectance and TOC data from the Norwegian Petroleum Directorate (NPD) and a  
344 previous study (Aarnes et al., 2015) are used to benchmark the model and match very well with the modelled  
345 results (Figure 7). Further information about the geological and model setting can be found in Aarnes et al.  
346 (2015) and the input file '1d\_sill\_input\_utgard.xlsx'.



347

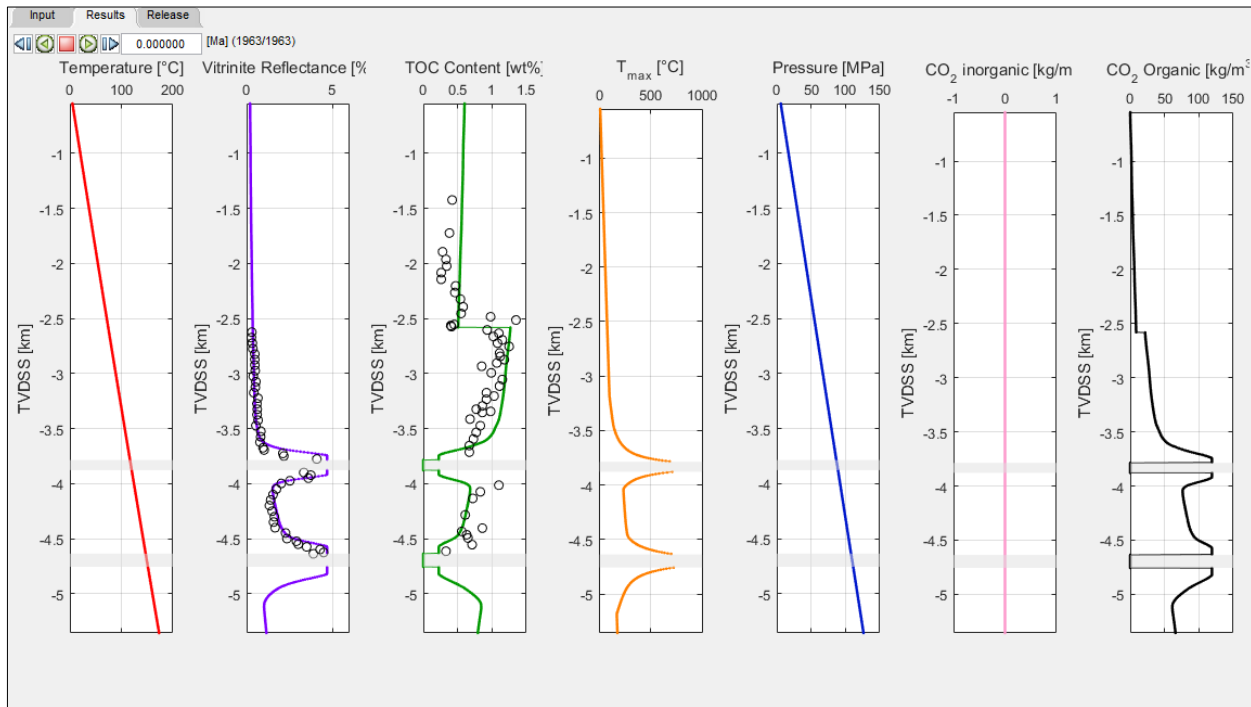
348 *Figure 5. Input tab for the Utgard High example.*



349

350 *Figure 6. Results tab 50 years after the emplacement of sills at 55 Ma for the Utgard High example. Sediments*  
351 *around the sills are heated and CO<sub>2</sub> is liberated as organic matter is thermally degraded.*

352



353

354 *Figure 7. Results tab at the end of simulation time for the Utgard High example. The present-day VR and TOC*  
355 *values (circles) show a good match with the model results.*

356

## 357 5.2 Example 2

358 The Karoo Large igneous province was emplaced through the Karoo Basin in South Africa in the Early Jurassic.  
359 The basin contains sills and dykes of varying thickness (Chevallier and Woodford, 1999; du Toit, 1920; Svensen  
360 et al., 2015; Walker and Poldervaart, 1949), emplaced at about 182.6 Ma (Svensen et al., 2012). The basin  
361 stratigraphy consists of the Upper Carboniferous to the Triassic Karoo Supergroup and is divided in five groups  
362 (the Dwyka, Ecca, Beaufort, Stormberg and Drakensberg groups) with a postulated maximum cumulative  
363 thickness of 12 km and a preserved maximum thickness of 5.5 km (Tankard et al., 2009). The depositional  
364 environments of the sediments range from marine and glacial (the Dwyka Group), marine to deltaic (the Ecca  
365 Group), to fluvial (the Beaufort Group) and finally eolian (the Stormberg Group) (Catuneanu et al., 1998). The  
366 Karoo Basin is overlain by 1.65 km of preserved volcanic rocks of the Drakensberg Group, consisting mainly of  
367 stacked basalt flows erupted in a continental and dry environment (e.g., (Duncan et al., 1984)). Several recent

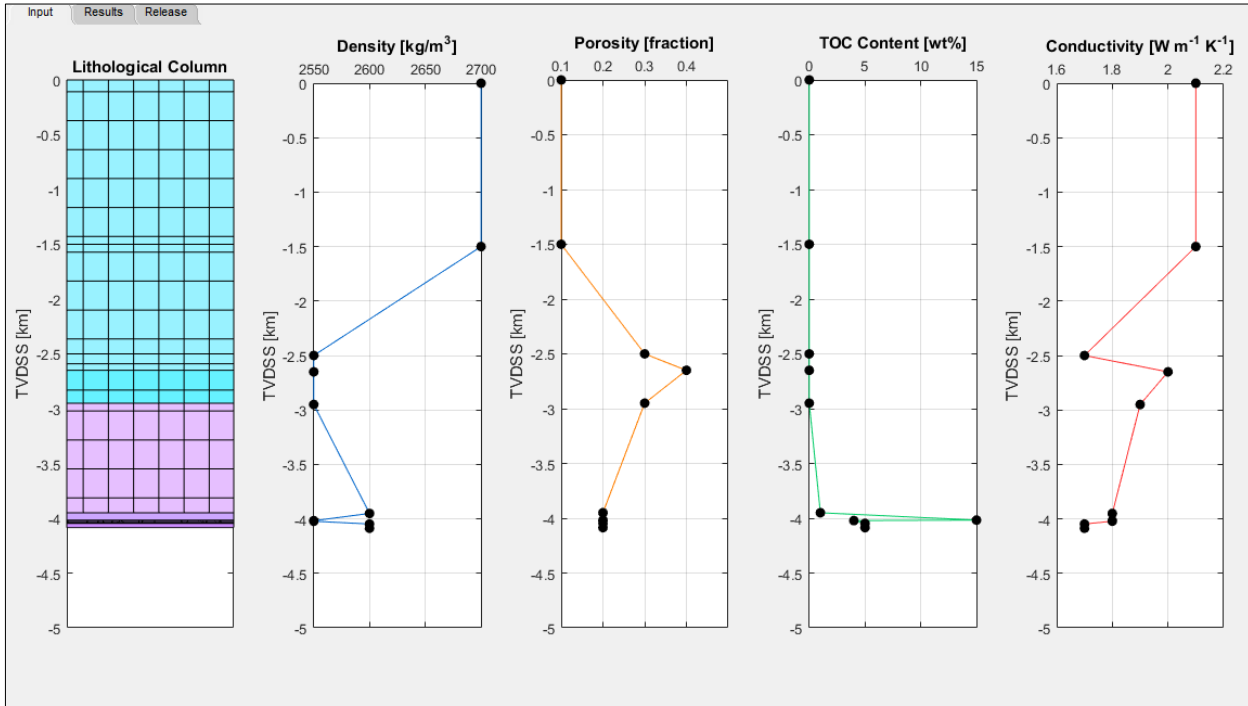


368 studies have been devoted to contact metamorphism of the organic-rich Ecca Group (Aarnes et al., 2011b;  
369 Moorcroft and Tonnelier, 2016) and the possible consequences of thermogenic methane venting on the Early  
370 Jurassic climate (Svensen et al., 2007; Svensen et al., 2015). Here we present two borehole cases from the  
371 central (borehole KL1/78) and eastern (borehole LA1/68) parts of the basin previously studied and modelled by  
372 Aarnes et al. (2011b) and Svensen et al. (2015), respectively. The details regarding the relative timing of sill  
373 emplacement is poorly constrained and we thus use the same age for all sills. If the sills are closely spaced, this  
374 will result in a higher maximum temperature in the sedimentary rocks between the sills (cf. (Aarnes et al.,  
375 2011b)). For the erosion history of the Karoo Basin, we refer to Braun et al. (2014) and a rapid Late Cretaceous  
376 erosion event.

### 377 **5.2.1 Karoo KL1/78**

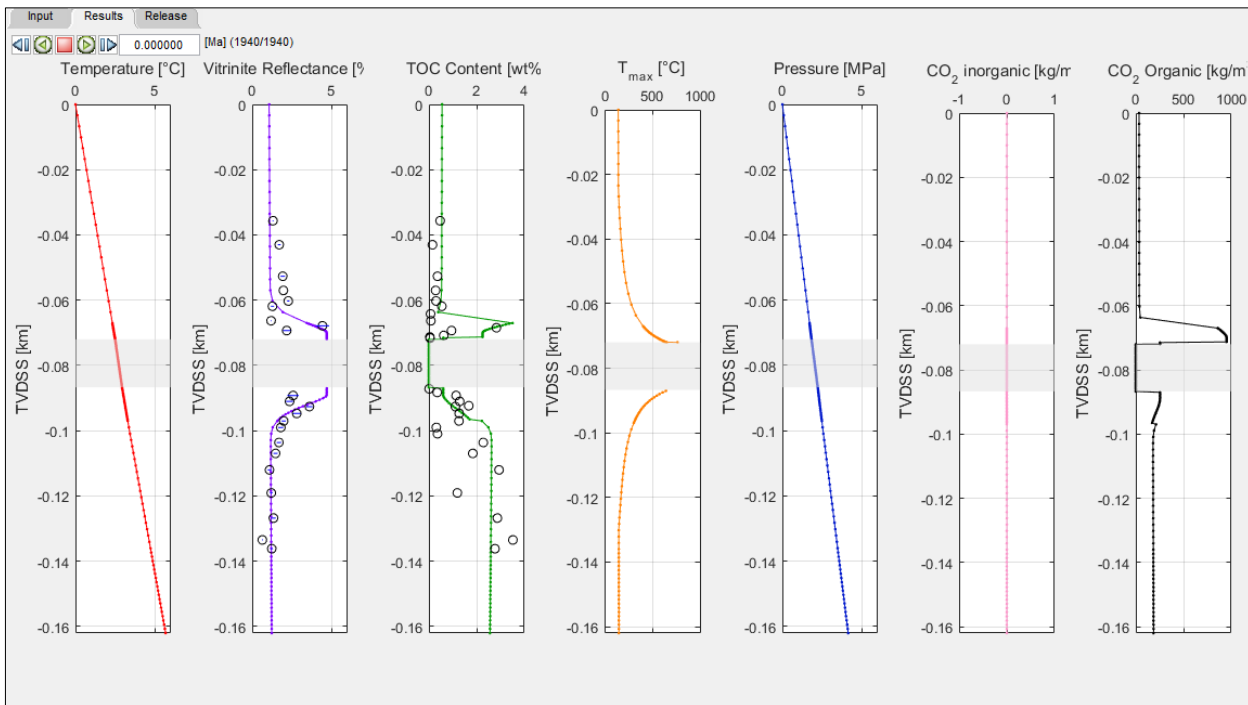
378 The first example from the Karoo Basin is a short borehole with a length of 136 m that penetrates the Tierberg,  
379 Whitehill and Prince Albert Formations. However, these Formations underlie a massive erosion sequence  
380 consisting of 2.5 km of extrusives (Drakensberg Group) and 1.5 km of sediments (Stormberg and Beaufort  
381 Groups) and are also included in the model. The borehole penetrates a single 15m thick sill at a depth of 72m  
382 (Figure 10). The sill is emplaced within the Prince Albert Formation at 182.6 Ma at a temperature of 1150°C.  
383 Initial average TOC data for the sedimentary layers is not known but can be roughly estimated using present-  
384 day values. The initial TOC data is subsequently refined so that a better match of the model results to the  
385 observed data is obtained, thereby highlighting how the model can be used to constrain initial conditions within  
386 the sedimentary column (Figure 11). The importance of considering the entire basin history when constructing  
387 the model is also emphasized by the VR results. The values of the VR results unaffected by the sill would be  
388 much lower than the observed values if the eroded sequences are not considered. Addition of these layers to  
389 the model results in added burial than would be expected than by just using the 136 m deep borehole. This  
390 translates the VR curve laterally thereby better fitting the observed values (Figure 11). The final model shows a  
391 good fit of TOC and VR to present day values. Model input data can be found in '1d\_sill\_input\_kl178.xlsx'.

392



393

394 *Figure 8. Input tab for KL178.*



395



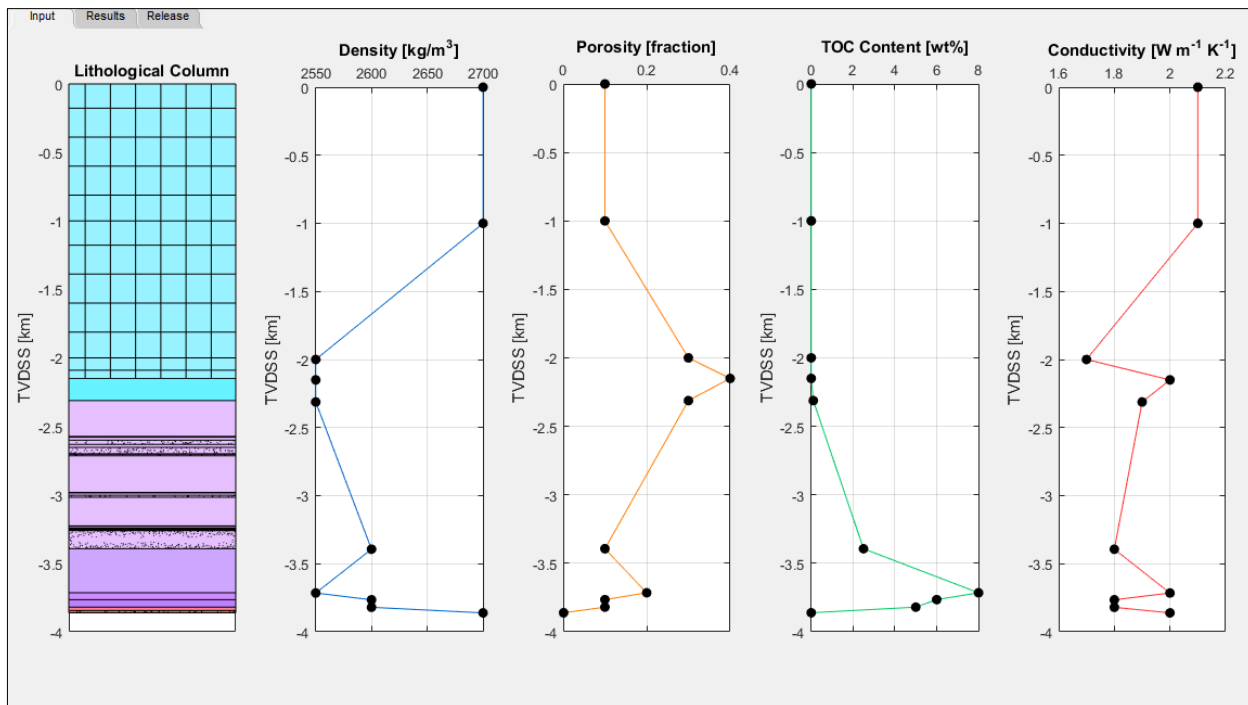


396 *Figure 9. Results tab at the end of simulation time for KL178 shows a good match to present-day TOC and VR*  
397 *values.*

398

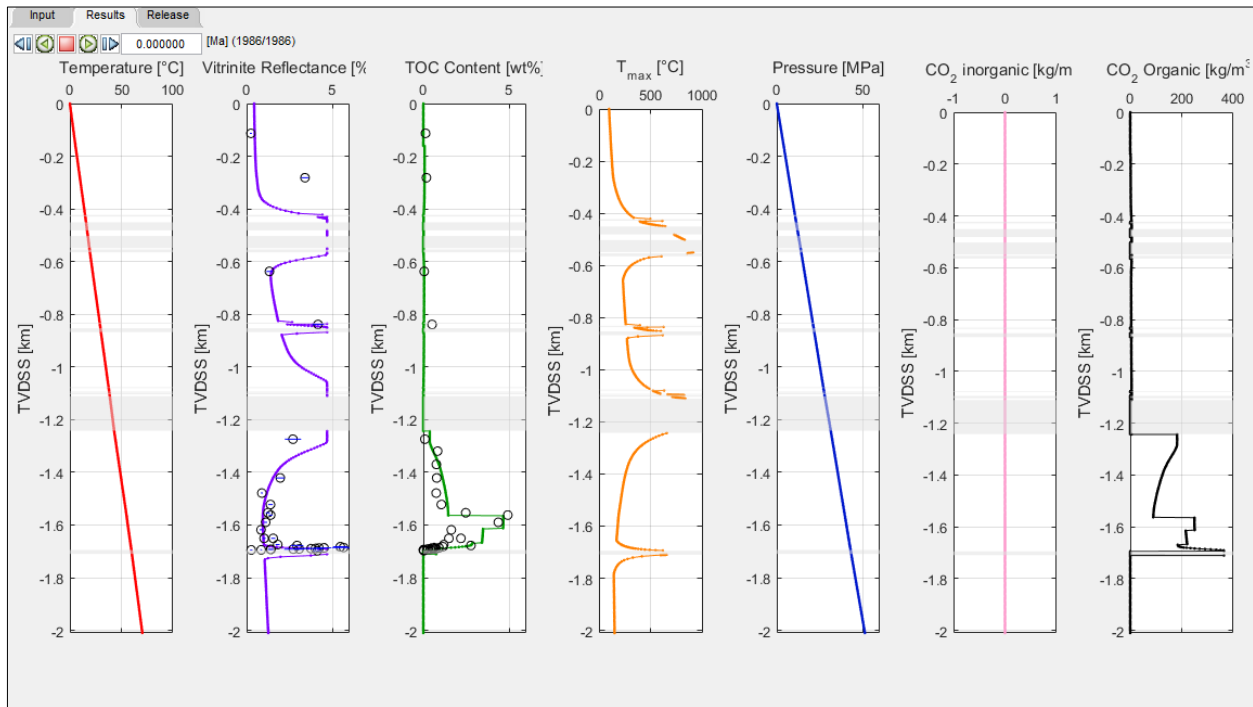
### 399 5.2.2 Karoo LA1/68

400 The second example from the Karoo Basin is a borehole with a length of 1711 m that penetrates the basin down  
401 to the basement (Svensen et al., 2015). Additional erosional sequence consisting mostly of the Drakensberg  
402 lavas and a minor section of the Stormberg Group is also added. The borehole penetrates multiple sills  
403 throughout the entire column with thicknesses ranging from 2 to 132m (Figure 10). Initial average TOC data for  
404 the sedimentary layers is estimated from present-day values. Similar to the previous example, material  
405 properties are iteratively changed within realistic bounds to arrive at an initial setup that matches the final  
406 observations well (Figure 11). Model input data can be found in '1d\_sill\_input\_la168.xlsx'.



407

408 *Figure 10. Input tab for LA168.*



409

410 *Figure 11. Results tab at the end of simulation time for LA168 shows a good match to present-day TOC and VR*  
411 *values.*

412

## 413 6 Conclusions

- 414 • SILLi is a numerical model quantifies the thermal evolution of contact aureoles around sills emplaced in  
415 sedimentary basins. The model includes basin history (burial and erosion), thus providing background-  
416 maturation levels of organic matter and consequently more realistic gas production estimates.
- 417 • SILLi is a user-friendly tool that is written in Matlab and uses Excel for input data.
- 418 • The 1D tool allows for the quick quantification of the thermal effects of sill intrusions. The results can  
419 be, therefore, used to further constrain and test the initial conditions that may have been present  
420 within the lithological column that match present-day observations.
- 421 • Model output includes peak temperature profiles, post-metamorphic TOC content, vitrinite reflectivity,  
422 and the cumulative amount and rate of CO<sub>2</sub> generation. These values can be readily upscaled to basin



423 scales if the sill extent is known. The amount of CO<sub>2</sub> can also be easily converted to other carbon-  
424 bearing gases such as CH<sub>4</sub>.

- 425 • Our three case studies demonstrate a good fit between aureole data (TOC and vitrinite reflectivity) and  
426 model output showing that the model can be successfully applied to basins in various global settings.

427

## 428 **7 Code Availability and Software Requirements**

429 The source code with examples is archived as a repository on Github/Zenodo (DOI:  
430 <https://doi.org/10.5281/ZENODO.803748>). Matlab 2014b or higher is required to run the code and Microsoft  
431 Excel or any equivalent software is required to edit .xls files.

432

## 433 **8 License (BSD-2-Clause)**

434 Copyright 2016 Karthik Iyer, Henrik Svensen and Daniel W. Schmid

435 Redistribution and use in source and binary forms, with or without modification, are permitted provided that  
436 the following conditions are met:

437 1. Redistributions of source code must retain the above copyright notice, this list of conditions and the following  
438 disclaimer.

439 2. Redistributions in binary form must reproduce the above copyright notice, this list of conditions and the  
440 following disclaimer in the documentation and/or other materials provided with the distribution.

441 THIS SOFTWARE IS PROVIDED BY THE COPYRIGHT HOLDERS AND CONTRIBUTORS "AS IS" AND ANY EXPRESS OR  
442 IMPLIED WARRANTIES, INCLUDING, BUT NOT LIMITED TO, THE IMPLIED WARRANTIES OF MERCHANTABILITY  
443 AND FITNESS FOR A PARTICULAR PURPOSE ARE DISCLAIMED. IN NO EVENT SHALL THE COPYRIGHT HOLDER OR  
444 CONTRIBUTORS BE LIABLE FOR ANY DIRECT, INDIRECT, INCIDENTAL, SPECIAL, EXEMPLARY, OR CONSEQUENTIAL  
445 DAMAGES (INCLUDING, BUT NOT LIMITED TO, PROCUREMENT OF SUBSTITUTE GOODS OR SERVICES; LOSS OF  
446 USE, DATA, OR PROFITS; OR BUSINESS INTERRUPTION) HOWEVER CAUSED AND ON ANY THEORY OF LIABILITY,  
447 WHETHER IN CONTRACT, STRICT LIABILITY, OR TORT (INCLUDING NEGLIGENCE OR OTHERWISE) ARISING IN ANY  
448 WAY OUT OF THE USE OF THIS SOFTWARE, EVEN IF ADVISED OF THE POSSIBILITY OF SUCH DAMAGE.



449 The software includes `errorbarxy.m` by Qi An (2016) (BSD-2-Clause License)  
450 (<http://www.mathworks.com/matlabcentral/fileexchange/40221>).

451

## 452 **9 Author Contributions**

453 K. Iyer and D.W. Schmid developed the code. K. Iyer implemented the code and wrote the manuscript. H.  
454 Svensen guided code development and provided input data from field studies. D. W. Schmid and H. Svensen  
455 edited the manuscript.

456

## 457 **10 Competing Interests**

458 The authors declare that they have no conflict of interest.

459

## 460 **11 References**

- 461 Aarnes, I., Fristad, K., Planke, S., and Svensen, H.: The impact of host-rock composition on devolatilization of  
462 sedimentary rocks during contact metamorphism around mafic sheet intrusions, *Geochem. Geophys. Geosyst.*,  
463 12, Q10019, 2011a.
- 464 Aarnes, I., Planke, S., Trulsvik, M., and Svensen, H.: Contact metamorphism and thermogenic gas generation in  
465 the Vøring and Møre basins, offshore Norway, during the Paleocene–Eocene thermal maximum, *Journal of the*  
466 *Geological Society*, doi: 10.1144/jgs2014-098, 2015. 588-598, 2015.
- 467 Aarnes, I., Svensen, H., Connolly, J. A. D., and Podladchikov, Y. Y.: How contact metamorphism can trigger global  
468 climate changes: Modeling gas generation around igneous sills in sedimentary basins, *Geochimica Et*  
469 *Cosmochimica Acta*, 74, 7179-7195, 2010.
- 470 Aarnes, I., Svensen, H., Polteau, S., and Planke, S.: Contact metamorphic devolatilization of shales in the Karoo  
471 Basin, South Africa, and the effects of multiple sill intrusions, *Chemical Geology*, 281, 181-194, 2011b.
- 472 Braun, J., Guillocheau, F., Robin, C., Baby, G., and Jelsma, H.: Rapid erosion of the Southern African Plateau as it  
473 climbs over a mantle superswell, *Journal of Geophysical Research: Solid Earth*, 119, 6093-6112, 2014.
- 474 Catuneanu, O., Hancox, P., and Rubidge, B.: Reciprocal flexural behaviour and contrasting stratigraphies: a new  
475 basin development model for the Karoo retroarc foreland system, *South Africa, Basin Research*, 10, 417-439,  
476 1998.
- 477 Chevallier, L. and Woodford, A.: Morpho-tectonics and mechanism of emplacement of the dolerite rings and  
478 sills of the western Karoo, South Africa, *S. Afr. J. Geol.*, 102, 43-54, 1999.
- 479 Connolly, J. and Petrini, K.: An automated strategy for calculation of phase diagram sections and retrieval of  
480 rock properties as a function of physical conditions, *Journal of Metamorphic Geology*, 20, 697-708, 2002.



- 481 du Toit, A. L.: the Karoo dolerites of south Africa: a study in hypabyssal injection, *S. Afr. J. Geol.*, 23, 1-42, 1920.
- 482 Duncan, A., Erlank, A., Marsh, J., and Cox, K.: Regional geochemistry of the Karoo igneous province, 1984. 1984.
- 483 Fjeldskaar, W., Helset, H. M., Johansen, H., Grunnaleiten, I., and Horstad, I.: Thermal modelling of magmatic  
484 intrusions in the Gjallar Ridge, Norwegian Sea: implications for vitrinite reflectance and hydrocarbon  
485 maturation, *Basin Research*, 20, 143-159, 2008.
- 486 Galushkin, Y. I.: Thermal effects of igneous intrusions on maturity of organic matter: A possible mechanism of  
487 intrusion, *Organic Geochemistry*, 26, 645-658, 1997.
- 488 Iyer, K., Rüpke, L., and Galerne, C. Y.: Modeling fluid flow in sedimentary basins with sill intrusions: Implications  
489 for hydrothermal venting and climate change, *Geochemistry, Geophysics, Geosystems*, 14, 5244-5262, 2013.
- 490 Iyer, K., Schmid, D. W., Planke, S., and Millett, J.: Modelling hydrothermal venting in volcanic sedimentary  
491 basins: Impact on hydrocarbon maturation and paleoclimate, *Earth and Planetary Science Letters*, 467, 30-42,  
492 2017.
- 493 Jaeger, J.: Thermal effects of intrusions, *Reviews of Geophysics*, 2, 443-466, 1964.
- 494 Jaeger, J. C.: The temperature in the neighborhood of a cooling intrusive sheet, *Am J Sci*, 255, 306-318, 1957.
- 495 Jaeger, J. C.: Temperatures outside a cooling intrusive sheet, *Am J Sci*, 257, 44-54, 1959.
- 496 Jamtveit, B., Bucher-Nurminen, K., and Stijfhoorn, D. E.: Contact Metamorphism of Layered Shale-Carbonate  
497 Sequences in the Oslo Rift: I. Buffering, Infiltration, and the Mechanisms of Mass Transport, *Journal of*  
498 *Petrology*, 33, 377-422, 1992.
- 499 Jamtveit, B., Svensen, H., Podladchikov, Y. Y., and Planke, S.: Hydrothermal vent complexes associated with sill  
500 intrusions in sedimentary basins. In: *Physical Geology of High-Level Magmatic Systems*, Breikreuz, C. and  
501 Petford, N. (Eds.), Geological Society Special Publication, Geological Soc Publishing House, Bath, 2004.
- 502 Kjøberg, S., Schmiedel, T., Planke, S., Svensen, H. H., Millett, J. M., Jerram, D. A., Galland, O., Lecomte, I.,  
503 Schofield, N., and Haug, Ø. T.: 3D structure and formation of hydrothermal vent complexes at the Paleocene-  
504 Eocene transition, the Møre Basin, mid-Norwegian margin, *Interpretation*, 5, SK65-SK81, 2017.
- 505 Lovering, T.: Theory of heat conduction applied to geological problems, *Geological Society of America Bulletin*,  
506 46, 69-94, 1935.
- 507 Malthe-Sorensen, A., Planke, S., Svensen, H., and Jamtveit, B.: Formation of saucer-shaped sills. In: *Physical*  
508 *Geology of High-Level Magmatic Systems*, Breikreuz, C. and Petford, N. (Eds.), Geological Society Special  
509 Publication, Geological Soc Publishing House, Bath, 2004.
- 510 Monreal, F. R., Villar, H. J., Baudino, R., Delpino, D., and Zencich, S.: Modeling an atypical petroleum system: A  
511 case study of hydrocarbon generation, migration and accumulation related to igneous intrusions in the  
512 Neuquen Basin, Argentina, *Marine and Petroleum Geology*, 26, 590-605, 2009.
- 513 Moorcroft, D. and Tonnelier, N.: Contact Metamorphism of Black Shales in the Thermal Aureole of a Dolerite Sill  
514 Within the Karoo Basin. In: *Origin and Evolution of the Cape Mountains and Karoo Basin*, Springer, 2016.
- 515 Pepper, A. S. and Corvi, P. J.: Simple kinetic models of petroleum formation. Part I: oil and gas generation from  
516 kerogen, *Marine and Petroleum Geology*, 12, 291-319, 1995.
- 517 Planke, S., Rasmussen, T., Rey, S. S., and Myklebust, R.: Seismic characteristics and distribution of volcanic  
518 intrusions and hydrothermal vent complexes in the Vøring and Møre basins. In: *Petroleum Geology: North-*  
519 *western Europe and global perspectives - Proceedings of the 6th Petroleum Geology Conference.*, Doré, A. G.  
520 and Vining, B. A. (Eds.), Geological Society, London, 2005.
- 521 Svensen, H., Corfu, F., Polteau, S., Hammer, O., and Planke, S.: Rapid magma emplacement in the Karoo Large  
522 Igneous Province, *Earth and Planetary Science Letters*, 325, 1-9, 2012.



- 523 Svensen, H. and Jamtveit, B.: Metamorphic Fluids and Global Environmental Changes, *ELEMENTS*, 6, 179-182,  
524 2010.
- 525 Svensen, H., Planke, S., Chevallier, L., Malthe-Sørenssen, A., Corfu, F., and Jamtveit, B.: Hydrothermal venting of  
526 greenhouse gases triggering Early Jurassic global warming, *Earth and Planetary Science Letters*, 256, 554-566,  
527 2007.
- 528 Svensen, H., Planke, S., Malthe-Sørenssen, A., Jamtveit, B., Myklebust, R., Rasmussen Eidem, T., and Rey, S. S.:  
529 Release of methane from a volcanic basin as a mechanism for initial Eocene global warming, *Nature*, 429, 542-  
530 545, 2004.
- 531 Svensen, H., Planke, S., Polozov, A. G., Schmidbauer, N., Corfu, F., Podladchikov, Y. Y., and Jamtveit, B.: Siberian  
532 gas venting and the end-Permian environmental crisis, *Earth and Planetary Science Letters*, 277, 490-500, 2009.
- 533 Svensen, H. H., Planke, S., Neumann, E.-R., Aarnes, I., Marsh, J. S., Polteau, S., Harstad, C. H., and Chevallier, L.:  
534 Sub-Volcanic Intrusions and the Link to Global Climatic and Environmental Changes, 2015. 2015.
- 535 Sweeney, J. and Burnham, A. K.: Evaluation of a simple model of vitrinite reflectance based on chemical kinetics,  
536 *AAPG Bulletin*, 74, 1559-1570, 1990.
- 537 Tankard, A., Welsink, H., Aukes, P., Newton, R., and Stettler, E.: Tectonic evolution of the Cape and Karoo basins  
538 of South Africa, *Marine and Petroleum Geology*, 26, 1379-1412, 2009.
- 539 Tracy, R. J. and Frost, B. R.: Phase equilibria and thermobarometry of calcareous, ultramafic and mafic rocks,  
540 and iron formations, *Reviews in Mineralogy and Geochemistry*, 26, 207-289, 1991.
- 541 Walker, F. and Poldervaart, A.: Karroo dolerites of the Union of South Africa, *Geological Society of America*  
542 *Bulletin*, 60, 591-706, 1949.
- 543 Wang, D. Y.: Comparable study on the effect of errors and uncertainties of heat transfer models on quantitative  
544 evaluation of thermal alteration in contact metamorphic aureoles: Thermophysical parameters, intrusion  
545 mechanism, pore-water volatilization and mathematical equations, *International Journal of Coal Geology*, 95,  
546 12-19, 2012.
- 547 Wang, D. Y., Lu, X. C., Song, Y. C., Shao, R., and Qi, T. A.: Influence of the temperature dependence of thermal  
548 parameters of heat conduction models on the reconstruction of thermal history of igneous-intrusion-bearing  
549 basins, *Computers & Geosciences*, 36, 1339-1344, 2010.
- 550 Wang, D. Y. and Song, Y. C.: Influence of different boiling points of pore water around an igneous sill on the  
551 thermal evolution of the contact aureole, *International Journal of Coal Geology*, 104, 1-8, 2012.
- 552 Wang, D. Y., Song, Y. C., Liu, Y., Zhao, M. L., Qi, T., and Liu, W. G.: The influence of igneous intrusions on the  
553 peak temperatures of host rocks: Finite-time emplacement, evaporation, dehydration, and decarbonation,  
554 *Computers & Geosciences*, 38, 99-106, 2012a.
- 555 Wang, K., Lu, X. C., Chen, M., Ma, Y. M., Liu, K. Y., Liu, L. Q., Li, X. Z., and Hu, W. X.: Numerical modelling of the  
556 hydrocarbon generation of Tertiary source rocks intruded by doleritic sills in the Zhanhua depression, Bohai Bay  
557 Basin, China, *Basin Research*, 24, 234-247, 2012b.